

Research Article

Dynamic Response Characteristics of the Electric Domain Structure of Ferroelectric Materials to the Surrounding Rock Structure of a Heavy-Duty Railway with a Small-Clearance Crossing Tunnel

Xiaotian Hao^{1,2} and Hailong Wang^{1,3} 

¹School of Traffic and Transportation, Shijiazhuang Tiedao University, Shijiazhuang, 050043 Hebei, China

²School of Urban Construction Engineering, Chongqing Technology and Business Institute, Chongqing 400052, China

³School of Civil Engineering, Hebei University of Architecture, Zhangjiakou, 075000 Hebei, China

Correspondence should be addressed to Hailong Wang; bhxt196346@cqtbi.edu.cn

Received 3 March 2022; Revised 28 June 2022; Accepted 12 July 2022; Published 12 August 2022

Academic Editor: Awais Ahmed

Copyright © 2022 Xiaotian Hao and Hailong Wang. This is an open access article distributed under the Creative Commons Attribution License, which permits unrestricted use, distribution, and reproduction in any medium, provided the original work is properly cited.

At present, the world-wide heavy-haul transportation technology of cargo trains has developed rapidly. Heavy-haul railway transportation has received extensive attention due to its large capacity, high efficiency, and low transportation costs. In order to understand the role that ferroelectric materials can play in the dynamic response of a heavy-duty railway surrounding rock structures in crosstunnels, this article introduces the domain structure of ferroelectric materials, derives the calculation method of the dynamic response of the surrounding rock structure, simulates the dynamic response characteristics through the corresponding formula, and analyzes the changes of the heavy-duty railway in the presence and absence of water. The situation was analyzed. The research results found that the increase of axle load will increase the bending moment of the invert structure. When the axle load is 30 t, the V-class surrounding rock is the most unfavorable working condition and the bending moment value of the invert structure is the largest at this time. When the added value of contact pressure is generally around 6.5 kPa, the railway as a whole can maintain a stable state.

1. Introduction

With the continuous improvement of my country's railway network, "passenger high speed" and "freight heavy duty" have become the two important directions of today's railway development. The structural stress forms and disease characteristics of heavy-duty railway tunnels are very different from those of ordinary railway tunnels. The bottom of the tunnel is the foundation that bears the load of trains and structures. Coupled with the effect of geological factors such as groundwater, the diseases at the bottom of the tunnel are particularly prominent, manifesting as lining cracks, venting and sinking of the basement, external squeezing of the side ditch, and mud and mud. Damage to the tunnel bottom causes a decrease in the safety reserve of the tunnel structure

in terms of strength, rigidity, and stability. These diseases not only endanger driving safety and deteriorate driving conditions but also increase tunnel maintenance costs and shorten tunnel service life.

Ferroelectric materials have some very excellent properties, such as dielectric properties. Ferroelectric materials include layered ferroelectric ceramics, relaxor ferroelectric ceramics, and antiferroelectric ceramics. When there is an external electric field, the positive and negative charges inside the ferroelectric material will shift to a certain extent, which will cause the charge centers to no longer overlap, and the so-called dipoles will appear. The applied electric field can drive the polarization direction of the dipole to move in the direction of the applied electric field, resulting in dielectric polarization. If we place a uniform dielectric

between the two poles of a capacitor, under the polarization of this dielectric, the capacitance value of the capacitor will increase several times compared with the capacitance value of the vacuum medium. This property is called dielectric. Ferroelectrics have the characteristics of large dielectric constant and obvious nonlinear effects. The spontaneous polarization of ferroelectric materials originates from the electric dipole generated by the noncoincidence of the positive and negative charge centers inside the unit cell. Perovskite structure ferroelectrics are currently the most widely studied, simplest, and most representative ferroelectric materials.

For the related applications of ferroelectric materials and the characteristics of railway dynamic response, experts at home and abroad have done a lot of research. In order to study the mechanism behind the collapse evolution, Xiao et al. conducted in situ microseismic (MS) monitoring in the left main/auxiliary power house. The temporal and spatial characteristics of stress-structure-controlled collapse are summarized and introduced. These methods provide a consistent set of results, that is, tensile fracturing is the most active rock mass fracturing mechanism in the evolution of stress-structure-controlled collapse. In addition, the evolution of microseismic activity during the development of the study collapse was also obtained. The results provide a direct case history, which will help predict and support stress-structure-controlled collapse disasters and help excavate deep-buried caves on site [1]. He et al. proposed an innovative roof-cutting and pressure-relief technology in response to the complex construction technology and high roadway construction costs in the traditional technology of retaining lanes along the goaf. A number of mechanical models of the “surrounding rock structure-roadside support” were established, and the design formulas for the support resistance of each roadway were obtained. The results show that through presplitting blasting, the lower foundation roof falls enough to better support the upper roof, thereby limiting the rotation deformation of the upper roof and reducing the impact load of the roof fracture [2]. Yan et al. deal with several types of inclination rail defects by simulating the acceleration system installed on the locomotive and theoretically study the feasibility of monitoring the inclination rail joint defects. The quantitative relationship between the axle box acceleration characteristics (peak) and the rail defects was determined by simulation. Therefore, the proposed method combines defect analysis and comparison with theoretical results, will enhance the ability of long-term monitoring and evaluation of the track system, and provide a more sensible preventive track maintenance strategy [3]. Cai et al. comprehensively studied the new track dynamics behavior of a polyurethane foam-cured ball in heavy-duty railway tunnels. First, based on the multibody system dynamics theory and finite element method, a dynamic model of the vehicle-track-tunnel interaction system is established. Then, the dynamic effect of the polyurethane foam-cured road ast track on the train and surrounding infrastructure is calculated and compared with the dynamic effect of the traditional road ast track [4]. In order to study the adaptability of cement-modified expansive soil as a filling material for heavy-duty railway subgrades, Cai et al. carried out different

axle loads, trains, speeds, and service environmental conditions based on the test section of the cement-modified expansive soil subgrade of the Menggan Railway. The results show that the dynamic parameters decay linearly along the depth and lateral direction of the subgrade in the same infill structure layer. The dynamic stress attenuation at the bottom of the subgrade surface is about 49%, and the dynamic stress attenuation at the bottom of the lowest subgrade is 76% [5]. Based on the train longitudinal dynamics theory and the vehicle-track coupling dynamics theory, Liu et al. established a heavy-duty train-track coupling dynamics model considering the longitudinal, lateral, and vertical forces of the coupler and traction system. The inspection conditions and mechanical properties of the locomotive under traction and braking conditions are analyzed, and the process and extent of the influence of traction, braking force, and coupler force on the locomotive performance are studied, and the theoretical model is verified by train [6]. The focus of Holder et al.’s research is the laboratory characterization of the lateral load path through the Skl-type fastening system using new instrument technologies that are subjected to heavy freight rail loading conditions. The investigation of the performance of the fastener system includes the evaluation of the lateral load distribution through the superstructure of the track and the evaluation of the single fastener system. The observations of this study will help the railway industry to improve the design of fastener systems and develop mechanical track structure design methods [7]. These studies have provided some references for this article, but due to certain problems in related research methods and data, the results of the experiment have not been accepted by the public.

The innovation of this article is that the article puts forward the theoretical calculation method of the surface load of the ballast bed based on the measured data combined with the existing specifications and the research results at home and abroad according to the characteristics of the ballast bed and the wheel-rail action mode. The elastic layered system is used to derive the elastic mechanics analytical solution of the surface load of the invert structure, which is an elastic foundation beam. The model and the load structure model provide the initial conditions of the load.

2. Response Characteristic Analysis Method

2.1. Ferroelectric Materials. A ferroelectric material is a kind of dielectric material. It has spontaneous polarization in two or more directions within a certain temperature range, and its spontaneous polarization will occur with the direction and magnitude of the external field (common electric field, temperature field). When the ferroelectric is below the critical temperature, it will transform from the paraelectric phase to the ferroelectric phase. This critical temperature is the Curie temperature (CT) [8, 9]. Figure 1 shows the change in the crystal structure of a ferroelectric material with a perovskite structure from a paraelectric phase to a ferroelectric phase. The general formula of perovskite is ABO_3 ; A and B are metal ions, and O is oxygen ion. Above the Curie temperature, the perovskite ferroelectric material has a cubic

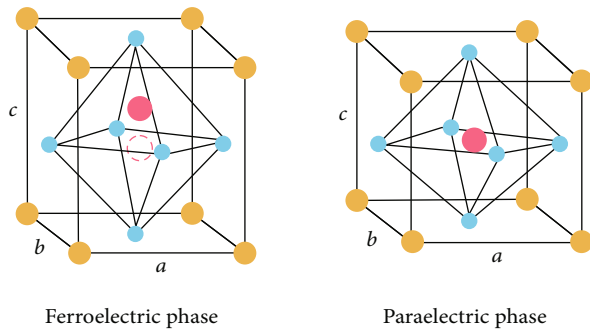


FIGURE 1: The crystal structure from the paraelectric phase to the ferroelectric phase of the perovskite structure.

crystal structure. At this time, the positive and negative charge centers coincide and the ferroelectric material is in a nonpolarized state, that is, the paraelectric phase; when the temperature drops below the Curie temperature, the atoms in the unit cell will move the ferroelectric material. Due to the different displacements of the positive and negative ions, the positive and negative charge centers no longer overlap, resulting in an electric dipole moment. Polarization refers to the electric dipole moment per unit volume, that is, at the Curie temperature. The following ferroelectric materials exhibit ferroelectricity in the macroscopic view [10].

As a kind of dielectric material, a ferroelectric material has other characteristics besides showing ferroelectricity, such as dielectric, piezoelectricity, pyroelectricity, photoelectric effect, acousto-optic effect, and optical transition effect [11]. These different characteristics also make ferroelectric materials have a wide range of applications. In the application of ferroelectric materials, ferroelectric memory uses the polarized bistable state for information storage, so it has the advantages of nonvolatile, fast reading and writing, fatigue resistance, radiation resistance, etc. and is considered to be one of the most potential new types of memory at present; ferroelectric memory has been commercialized [12]. The hysteresis loop of ferroelectric materials is shown in Figure 2.

Important parameters such as spontaneous polarization CP, remanent polarization OP, coercive field BG, and ferroelectric loss can be obtained by measuring the hysteresis loop. It is precisely because of these advantages that ferroelectric memory has been widely used in both civilian and military fields [13, 14]. Ferroelectric memory is currently the only new-generation memory that has been widely used, and its advantages and application areas are shown in Figure 3.

Ferroelectric memory allows designers to write data to nonvolatile memory faster and more frequently and at a lower price. The failure of the ferroelectric thin film is caused by the abnormal evolution of the ferroelectric single domain. The essential reasons for determining ferroelectric domains and domain flipping are the microstructure of ferroelectric thin films such as lattice defects, interface terminal types, and oxygen vacancies [15]. With the miniaturization and high integration of ferroelectric memory, the size of ferroelectric thin films in the thickness direction is close to

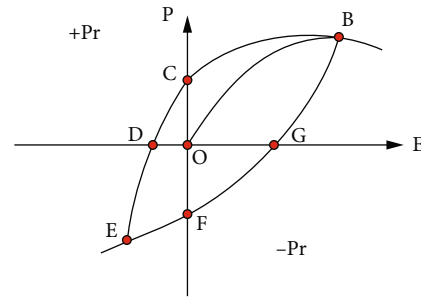


FIGURE 2: Schematic diagram of hysteresis loop of ferroelectric material.

the nanometer scale and the polarization/domain structure and evolution are increasingly restricted by the abovementioned factors.

2.2. Heavy-Duty Railway Tunnel Structure. The tunnel bottom structure is the main load-bearing structure of heavy-duty railway tunnels, and the load size is mostly determined based on the experience of ordinary railway tunnels. The accurate theoretical calculation method can quickly calculate the dynamic load on the surface of each structural layer and determine the initial load conditions of the calculation model, which has important guiding significance for the design of heavy-duty railway tunnels [16].

Based on the force mode of the track bed structure of the heavy-duty railway tunnel under the action of sleepers, a calculation method for the dynamic load on the sleeper bottom surface is proposed, that is, the static axle load/wheel weight is converted to the dynamic axle load/wheel load according to the train speed, combined with the contact area of the sleeper bottom surface. The additional value threshold of the dynamic load caused by the train is calculated.

$$\sigma = \frac{P * (1 + \beta v)}{BL}, \quad (1)$$

where σ is the stress, P is the static axle load, and β is the dynamic impact coefficient, also known as the velocity influence coefficient.

The dynamic load on the surface of the track bed structure is calculated according to formula (1), which is different from the actual “saddle-shaped” or “triangular” load distribution on the surface of the track bed structure. The error is compensated [17]. Table 1 compares the calculated results of formula (1) with the measured dynamic load threshold on the surface of the track bed structure.

According to D'Alembert's principle, the dynamic differential equation of the structure can be obtained as follows:

$$[M]\{\ddot{\phi}\} + [C]\{\dot{\phi}\} + [K]\{\phi\} = [F(t)]. \quad (2)$$

Among them, M stands for the mass matrix, C stands for the damping matrix, K stands for the stiffness matrix, and ϕ stands for displacement.

Regarding the formula as a constant coefficient differential equation, the displacement of the structure can be used

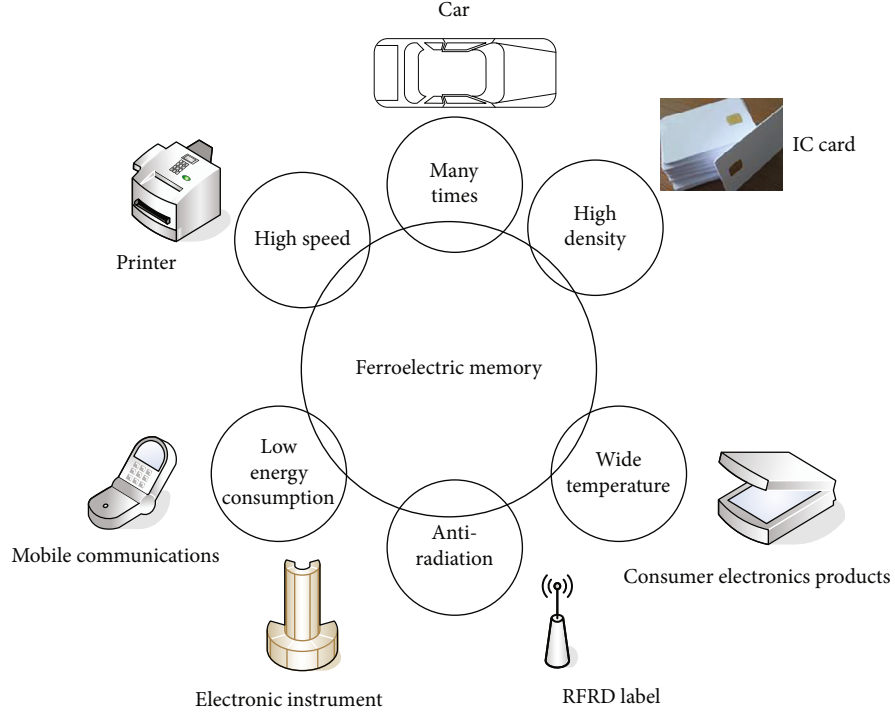


FIGURE 3: Ferroelectric memory application.

TABLE 1: Comparison of calculation results and formulas.

Surrounding rock level	Train axle weight (ton)	Tunnel form	Cumulative dynamic load threshold	Formula calculated value
III	26	Single-line ballastless	81.6	425.44
		Double-line ballast	143.2	425.44
			125.6	425.44
IV	26	Two-wire ballastless	129.5	425.44
	29		163.3	532.74
V	26		120.1	425.44
	29		164.1	532.74

to approximate the velocity and acceleration of the structure through a finite difference expression. One of the most effective solutions is the central difference method. The method assumes

$$\begin{aligned}\{\phi\} &= \frac{1}{\Delta t^2} (\{\phi_{t-\Delta t}\} - 2\{\phi\} + \{\phi_{t+\Delta t}\}), \\ \{\phi_t\} &= \frac{1}{2\Delta t} (\{-\phi_{t-\Delta t}\} + \{\phi_{t+\Delta t}\}).\end{aligned}\quad (3)$$

Based on the abovementioned formula, we can get

$$\left(\frac{1}{\Delta t^2} [M] + \frac{1}{2\Delta t}\right) \{\phi_{t+\Delta t}\} = [F(t)] - \left([K] - \frac{2}{\Delta t^2} M\right). \quad (4)$$

The theoretical basis of the finite element method is the

weighted residual method and the variational method. The weighted margin method commonly used is the configuration method, the least square method, the moment method, and the Galerkin method, among which the Galerkin method is the most widely used. The variational method is aimed at solving the continuum problem. For the function of the unknown function, there are

$$\Pi = \int_{\gamma} F\left(u, \frac{\partial u}{\partial k}\right) d\gamma + \int_{\gamma} E\left(u, \frac{\partial u}{\partial x}\right) d\Gamma. \quad (5)$$

In the formula, u is an unknown function, F is a specific operator, and E is a specific operator.

Next, the discrete unit is determined, the finite element is divided, and the displacement interpolation function is determined. The matrix form is generally

$$u = \begin{pmatrix} u \\ v \end{pmatrix} = \begin{pmatrix} N_i & 0 \\ 0 & N_i \end{pmatrix} \begin{bmatrix} Ni & 0 & Nj \\ 0 & Ni & 0 \end{bmatrix} = [Ni, Nj, Nm]a^e. \quad (6)$$

In the formula, N is the interpolation function matrix and a^e is the nodal displacement matrix.

According to the element displacement obtained in the previous step, the stress-strain equation of each element can be solved according to the geometric and physical equations and the stress-strain matrix is obtained as follows:

$$\begin{aligned} \varepsilon &= \begin{pmatrix} \varepsilon_x \\ \varepsilon_y \\ \varepsilon_{xy} \end{pmatrix} = Lu = LNa^e = [Bi, Bj, Bm]a^e = Ba^e, \\ \sigma &= \begin{pmatrix} \sigma_x \\ \sigma_y \\ \sigma_{xy} \end{pmatrix} = D\varepsilon = DBa^e = Sa^e, \\ S &= DB = D[B_i, B_j, B_m] = [S_i, S_j, S_m]. \end{aligned} \quad (7)$$

In the formula, B is the strain matrix, L is the differential operator, S is the stress matrix, and D is the elastic matrix.

Based on the principle of virtual work, the stiffness matrix equation is established as follows:

$$\{F\}^e = [K]^e \{u\}^e. \quad (8)$$

In the formula, $\{F\}^e$ is the vector of the concentrated force on the nodes of the element, $[K]^e$ is the element stiffness matrix, and $\{u\}^e$ is the displacement vector of the element nodes.

The stepwise integration method is a kind of direct integration method. It uses finite difference instead of the derivative of displacement γ'' with γ'' respect to time and expresses the sum with the combination of displacements to obtain the recurrence formula of each time interval and then obtain the response of the entire time history. The content of the method is as follows:

γ' and γ'' can be expressed by displacement γ :

$$\begin{aligned} \gamma'' &= \frac{1}{\Delta t^2} (\delta_{t-\Delta t} - 2\delta_t + \delta_{t+\Delta t}), \\ \gamma' &= \frac{1}{2\Delta t} (-\delta_{t-\Delta t} + \delta_{t+\Delta t}). \end{aligned} \quad (9)$$

The recurrence formula of the stepwise integration method is as follows:

$$\left(\frac{1}{\Delta t^2} M + \frac{1}{2\Delta t} C \right) \delta_{t+\Delta t} = Qt - \left(K - \frac{2}{\Delta t^2} M \right) \delta_t. \quad (10)$$

The definition of the distance function is as follows for all $\vec{x}_1 \in \Gamma$:

$$d(\vec{x}) = \min \left(\left| \vec{x} + \vec{x}_1 \right| \right). \quad (11)$$

From the definition, when the unknown point is on the boundary, the function value is 0. Find the closest point on the boundary and mark the closest point and the value of the distance function is

$$d(\vec{x}) = \left| \vec{x} - \vec{x}_c \right|. \quad (12)$$

From the definition of the distance function, the specific definition of the signed distance function is

$$\begin{aligned} \phi(\vec{x}) &= d(-\vec{x}) = 0, \quad \vec{x} \in \Gamma, \\ \phi(\vec{x}) &= -d(\vec{x}), \quad \vec{x} \in \psi. \end{aligned} \quad (13)$$

The signed distance function is a subset of the implicit function and has all the properties of the implicit function discussed in the previous section [18]. Using the signed distance function can simplify many level set methods for dealing with implicit functions.

$$Z_i = T^T (x_{nm} - f \notin R^n). \quad (14)$$

Meet the orthogonal normalization condition, namely,

$$b_j^T b_k = \delta_{jk}, \quad (15)$$

in which, at the time, $j = k$, $\delta_{jk} = 1$; otherwise, $\delta_{jk} = 0$.

$$X'_{ij} = d + BB^T (X_{ij} - d) = d + BZ_j. \quad (16)$$

The formula is inverse transformation. In actual operation, due to the influence of noise data or different transformation methods, there are errors between them, as shown as follows:

$$\varepsilon_j = X_{ij} - X'_{ij} = X_{ij} - d - BB^T (X_{ij} - d). \quad (17)$$

The vibration load caused by train operation is generally a small amplitude load, and the shield tunnel lining and surrounding rock generally only undergo elastic deformation under the action of the train vibration load [19].

2.3. Heavy-Duty Railway. Chloride ions corrode the steel bars, resulting in the continuous loss of the effective cross-sectional area of the steel bars, and the load-bearing capacity is obviously reduced. The corrosion of the steel bars causes the rust expansion effect, causing the concrete protective layer to crack. The continuous development of the cracks also accelerates the corrosion of chloride salts and reduces the bearing capacity of the concrete. Chloride ions invade the reinforced concrete structure and severely reduce the bonding force between the steel bar and concrete, which will cause the steel bar and concrete to not work together normally [20, 21]. Therefore, the corrosive effect of chloride

ions is one of the main reasons that affect the service life of reinforced concrete structures.

Among the diseases of heavy-duty railway tunnels, the most frequent occurrence is water seepage diseases. Water leakage is the most common disease in well-known railway tunnels and has less harm to the tunnel structure. Therefore, the number of diseases at the bottom of the tunnel is ranked second, which is sufficient to explain the heavy-duty railway tunnels. The problem of the disease at the bottom of the tunnel is particularly prominent, which indicates that the bottom of the tunnel is the main place where the disease of the heavy-duty railway tunnel occurs. The conditions of the disease at the bottom of the tunnel are shown in Figure 4.

From the point of view of the location of the disease, different diseases occurred in the upper arch wall structure and the lower tunnel bottom structure of the heavy-duty railway tunnel [22]. Comparing the disease rates of passenger-cargo railway tunnels and heavy-duty railway tunnels, the disease rate of heavy-duty railway tunnels is much higher than the average disease rate of the whole road tunnel, indicating that the high disease rate of heavy-duty railway tunnels is its primary feature [23].

Because the heavy-duty train runs on continuous rails, the train vibration load generated by the interaction between the heavy-duty train and the rail is continuous in space and time. Then, the discrete fastener system distributed at a certain interval in the track structure converts the continuous excitation load on the upper part into multiple vertical excitation loads that act on specific positions of the track structure and then transfer them to the concrete track bed, and then, the track bed is transferred to the shield segment tunnel, and finally, the load is transferred to the soil layer [24]. Among them, under the action of the vibration load of the heavy-duty train, the vibration load curve of each fastener system can be obtained from the actual measurement situation [25].

Based on the vertical dynamics analysis model of the subway train in the shield tunnel, the vibration load of the subway train required for the similar model test is realized by applying a vertical excitation load on the position of the fastener on the concrete track bed and through multiple excitations. The device applies the fastener load at a certain time interval to simulate the effect of the train.

3. Response Characteristic Experiment and Results

3.1. Foundation Beam Calculation. Single-track heavy-duty railway tunnels and double-track heavy-duty railway tunnels are usually only equipped with the floor structure under the condition of level II surrounding rock. Therefore, this example is based on the Winkler foundation beam theory to analyze the single-track and double-track heavy-duty railways of level II surrounding rock. The internal force calculation of the tunnel was the floor structure. The internal force solution of the calculation model for the slab structure of the class II surrounding rock single-track tunnel under the action of 27 t axle load is shown in Table 2.

The theoretical calculation of the bending moment and shear force of the calculation model of the elastic foundation beam bottom plate of the single-track tunnel is shown in Table 3.

We list the converted concentrated loads corresponding to the characteristic points on the surface of the invert structure of the single-track tunnel under the condition of the 27 t axial load of the III-level surrounding rock. The boundary constraint conditions of the invert structure are considered in accordance with the consolidation, and the internal forces of the invert structure under different concentrated loads are solved. The overlay is shown in Table 4.

Then, the internal force of the invert structure under the action of concentrated force is solved and listed in Table 5.

It can be seen that the concentrated load of F1~F5 will cause the bending moment value of the corresponding characteristic point to increase. After the internal force is superimposed, it is found that the bending moment value of the single-track tunnel invert structure under the symmetrical load is also symmetrically distributed and the bending moment value at the center of the line maximum.

3.2. Dynamic Response Characteristic Analysis. Since the left amplitude of the surface load of the invert structure is larger than the right amplitude as a whole, the structural bending moments show the same regularity. The bending moment theory of the invert structure is obtained by summing the bending moments under the action of the equivalent 7 concentrated loads of the 27 t axle load calculated. We compare the theoretical calculation solution of the bending moment of the invert structure corresponding to different working conditions with the measured data, and the results are shown in Figures 5 and 6.

The measured data show that the decrease of surrounding rock conditions and the increase of axle load will increase the bending moment of the invert structure. When the axle load is 30 t, the V-level surrounding rock is the most unfavorable working condition and the bending moment value of the invert structure is the largest at this time. For the lateral distribution of the bending moment of the inverted arch structure, the value of the bending moment of the heavy-duty line, that is, the left line and the right rail position, is the largest and gradually decreases with the increase of the lateral distance. There is a certain error in the analysis of the bending moment under the most unfavorable conditions. According to the most unfavorable principle, it is considered that the calculation method of the curved elastic foundation beam can be applied to the design of the invert structure of the double-track heavy-duty railway tunnel.

The change curve of the additional value ΔP of the contact pressure of the no. 1 measuring point at the bottom left of the center line and the no. 2 measuring point below the center line with and without water is shown in Figure 7.

It can be seen that when the surrounding rock at the bottom of the tunnel is in anhydrous conditions, the additional value of contact pressure ΔP below the center line fluctuates at about 6.5 kPa and the additional value of contact pressure on the left and right side ΔP is stable at about 5.8 kPa but the

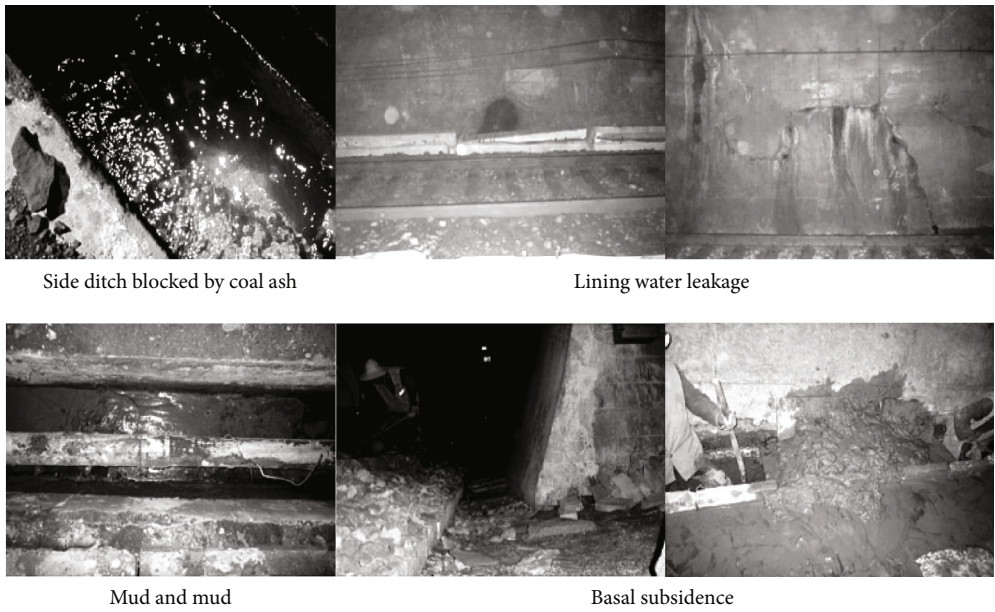


FIGURE 4: Classification of diseases in heavy-duty railway tunnels.

TABLE 2: Calculating model of the slab structure of the single-track tunnel in surrounding rock.

Internal solution	Feature location	q1-q2 load section		q2-q3 load section	
		Uniform load	Triangular load	Uniform load	Triangular load
Bending moment (KN*m)	Left sulcus	-11.13	-1.76	-4.01	-0.64
	Line left rail	3.72	0.74	0.41	0.11
	Line center	4.44	1.02	4.44	1.02
	Right track	0.41	0.11	3.72	0.74
	Right sulcus	-4.01	-0.64	-11.13	-1.76
	Left sulcus	-30.06	-3.31	-3.62	-0.52
Shear force (kM)	Line left rail	-9.02	-2.17	-5.21	-1.07
	Line center	5.44	1.09	-5.43	-1.09
	Right track	5.22	1.07	9.02	2.19
	Right sulcus	3.62	0.52	30.06	3.31

TABLE 3: Moment and shear force calculation model for elastic foundation beam bottom plate of single-track tunnel.

Axle load	Internal solution	Left sulcus	Line left rail	Line center	Right track	Right sulcus
27 t	Bending moment (KN*m)	-17.87	5.21	10.25	5.21	-17.87
	Shear force (kM)	-37.73	-16.71	0	16.71	37.73
30 t	Bending moment (KN*m)	-18.54	6.46	11.46	6.46	-18.45
	Shear force (kM)	-40.31	-17.01	0	17.01	40.31

TABLE 4: Characteristic points of single-track tunnel invert structure.

Serial number	Feature point location	C0	C1	C2	C3	C4	Bending moment (KN*m)
1	Left sulcus	-1.17E-03	1.17E-03	-1.42E-03	-2.56E-03	2.76E-03	1.53
2	Line left rail	-2.41E-03	2.41E-03	-3.01E-03	5.14E-03	-5.44E-03	4.31
3	Line center	-2.62E-03	2.62E-03	-3.16E-03	-5.58E-03	-6.01E-03	8.08
4	Right track	-2.41E-03	2.41E-03	-3.01E-03	-5.58E-03	-5.44E-03	4.31
5	Right sulcus	-2.62E-03	2.62E-03	-3.16E-03	-5.58E-03	-6.01E-09	1.53

TABLE 5: Calculation results of bending moment of surrounding rock invert structure.

Serial number	Feature point location	F1	F2	F3	F4	F5
1	Left sulcus	4.71	16.65	21.48	-2.01	-2.25
2	Line left rail	1.77	2.34	3.31	1.54	0.77
3	Line center	1.38	2.03	8.08	2.03	1.38
4	Right track	0.77	1.54	4.31	2.34	1.77
5	Right sulcus	0.76	1.02	1.63	1.86	1.29

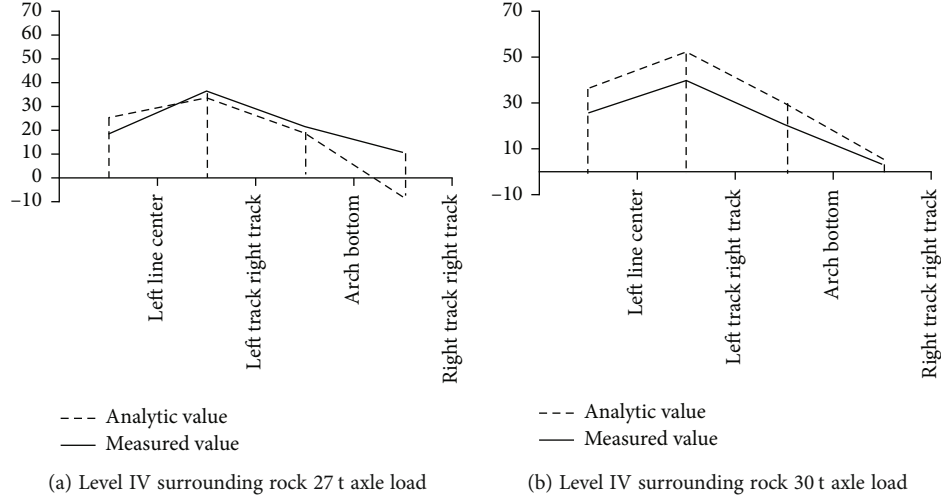


FIGURE 5: Bending moment of invert structure of class IV heavy-duty railway tunnel.

overall situation is relatively stable. The additional value of the contact pressure below the center line is slightly reduced compared with that below the center line, indicating that the effect of the excited vibration load below the center line is more obvious than that of other positions.

In order to understand the role of the domain structure of ferroelectric materials, we compare the elastic energy, depolarization energy, and various abilities of the ferroelectric material domain structure and the railway surrounding rock structure under traditional materials. The comparison result is shown in Figure 8.

It can be seen in Figure 8 that after comparing the elastic properties of different materials, it can be seen that the elastic properties of traditional materials vary greatly, and as the number of uses increases, their elastic properties must show a certain degree. In the case of ferroelectric materials, the elastic performance is much better than that of traditional materials and the increase rate is about 30%.

We compare the depolarization energies of the two materials, and the results are shown in Figure 9.

As can be seen, in the comparison of the depolarization energy of traditional materials and ferroelectric materials, the depolarization energy of traditional materials is much higher than that of ferroelectric materials and as the number of tests increases. The depolarization energy of traditional materials shows an upward trend, while the trend of ferroelectric materials shows a downward trend.

We compare the various abilities of the two materials, and the results obtained are shown in Figure 10.

It can be seen that for the supernatural power of materials, the difference between ferroelectric materials and traditional materials is not much. In this simulation test, there is no obvious difference between the values obtained by the two. This shows that ferroelectric materials have no special advantage over traditional materials in terms of abilities.

4. Discuss

4.1. Surrounding Rock Structure. Based on a variety of research methods such as the on-site large-scale in situ vibration test, long-term remote monitoring, theoretical derivation, numerical simulation, and data investigation, the dynamic characteristics, load theoretical calculation methods, calculation models, and fatigue damage evolution laws of heavy-duty railway tunnel structures are carried out. The dynamic response and stress distribution characteristics of different structural parts of heavy-duty railway tunnels are clarified.

The heavy-duty railway tunnel is divided into two major structural parts, the upper arch wall structure and the lower tunnel bottom structure, to analyze the dynamic response and stress distribution characteristics, respectively. The increase of the axle load of the heavy-duty train, the decrease of the surrounding rock conditions, and the decrease of the

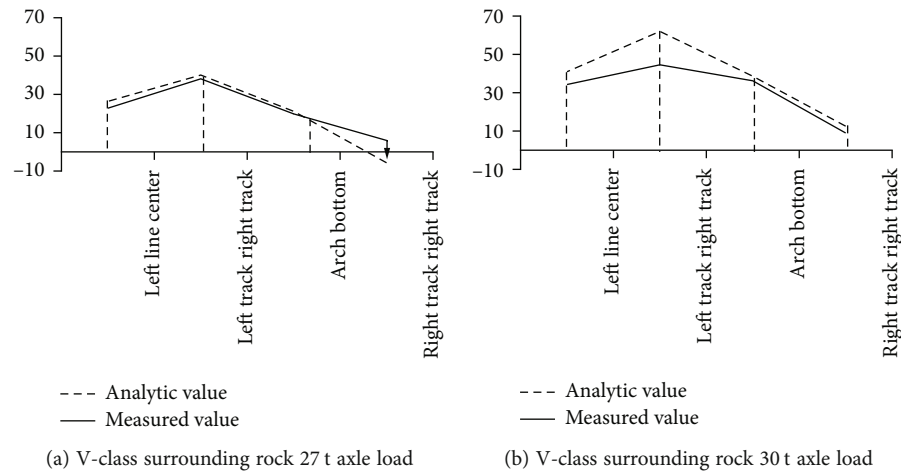


FIGURE 6: Bending moment of invert structure of V-class surrounding rock heavy-duty railway tunnel.

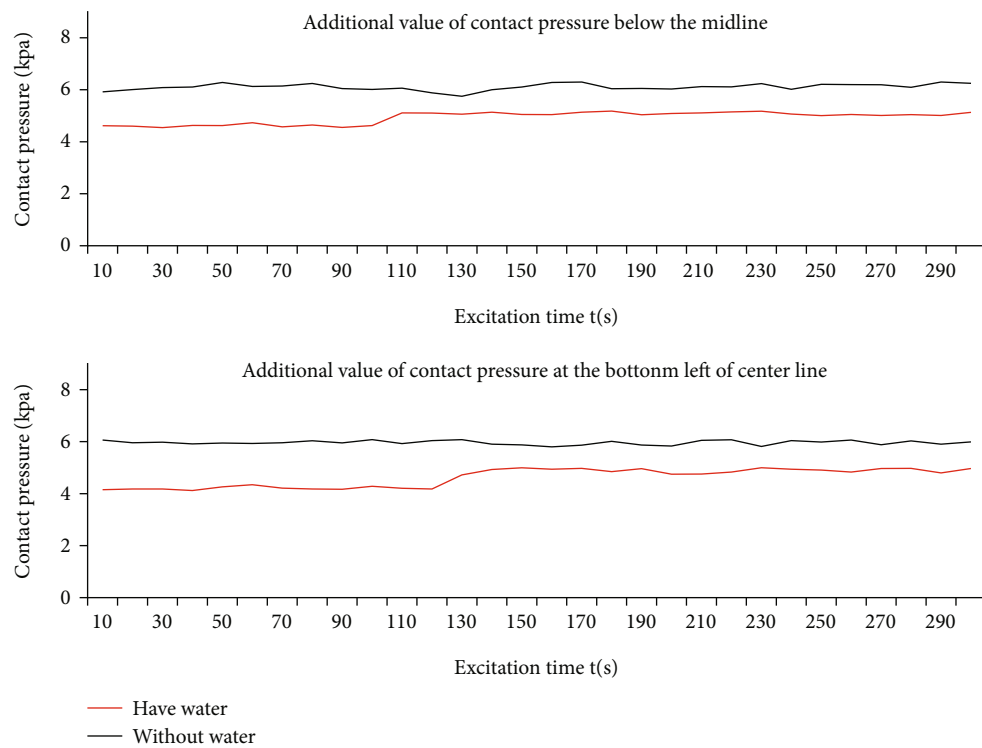


FIGURE 7: Pressure changes at the measuring point below the center line.

distance from the train load acting position will increase the dynamic load increment on the surface of the structure and the internal force of the structure.

The dynamic response and stress distribution characteristics of the arch wall structure are clarified: single- and double-line tunnels and ballastless and ballasted tunnel arch wall structures have similar dynamic load distribution laws under various working conditions and under the most unfavorable working conditions (class V) (surrounding rock, 30 t axle load). The maximum power increment does not exceed 5%, which is less affected by the power of heavy-duty trains.

The surface load distribution and vertical transmission laws of the various structural layers of the heavy-duty railway tunnel bottom structure are clarified: (1) the heavy-duty train load gradually decreases with the increase of the vertical depth during the transmission of the tunnel bottom structure, and the track bed structure has a large rigidity and a filling layer. The large thickness has a buffer effect on the dynamic load. When the dynamic load is transmitted to the surface of the surrounding rock, there has been a significant attenuation but the maximum power increase of the single-track tunnel is still 38.26% and 9.6% of the double-

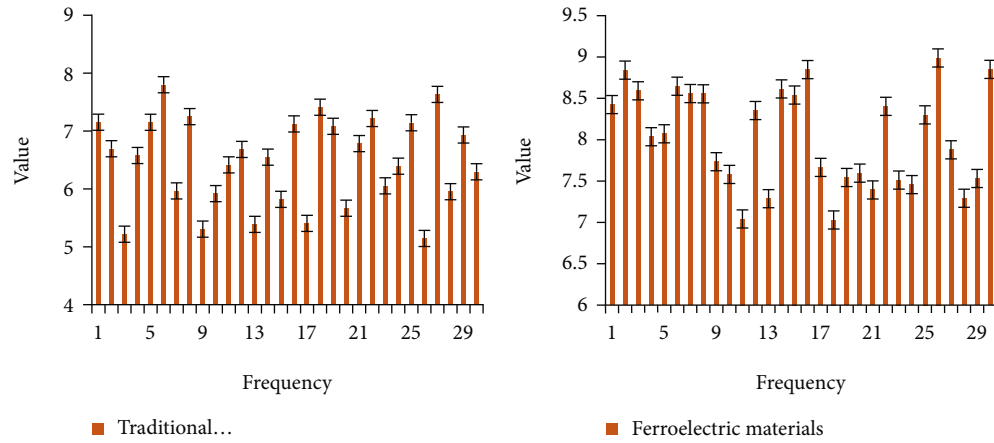


FIGURE 8: Comparison of elastic properties of different materials.

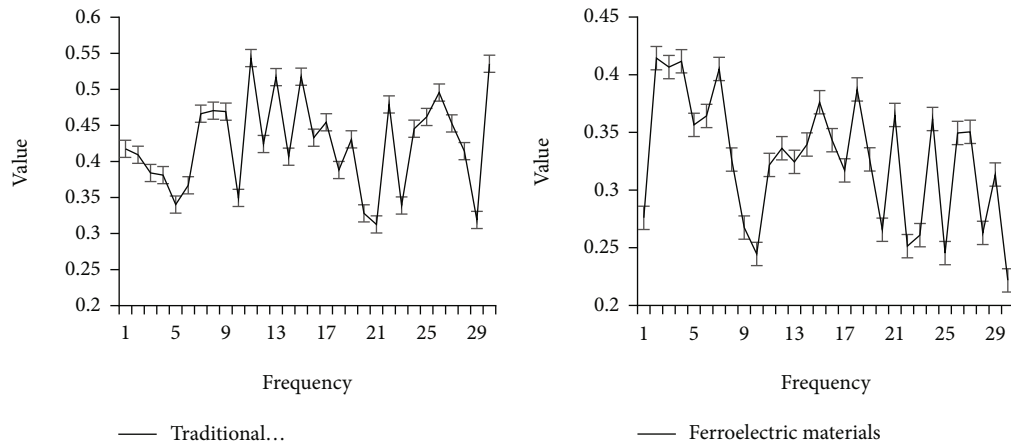


FIGURE 9: Comparison of depolarization energy.

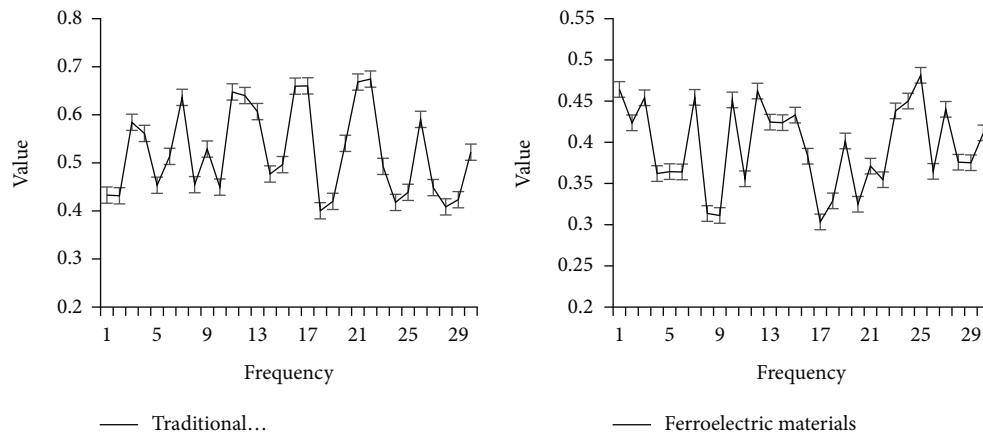


FIGURE 10: Comparison of various abilities.

track tunnel is much higher than the arch wall structure. Therefore, the dynamic impact of the heavy-duty train on the tunnel structure is mainly focused on the structure at the bottom of the tunnel. (2) In the single-track heavy-duty railway tunnel, due to the symmetry of the structure, the lateral distribution of the additional train load on the

surface of each structural layer at the bottom of the tunnel is in a “triangular” distribution, which is represented by the largest line center and gradually attenuates with the increase of the lateral distance. (3) In double-track ballasted and unballasted heavy-duty railway tunnels, the dynamic load distribution on the surface of the track bed, the surface

of the invert, and the surface of the surrounding rock shows that the dynamic effect of the train is mainly concentrated on the position of the track of the heavy-duty line. There is a difference in the dynamic load distribution on the surface of the two types of ballast beds. The surface of the filled layer of the ballastless bed is “saddle shaped,” and the ballast bed has a “triangular” load, and the dynamic load value of the ballast bed is higher than that of the ballastless bed. (4) The influence rate of the axle load on the dynamic increase of the tunnel bottom structure is up to 33.5%~48.2%, and the influence rate of surrounding rock conditions is up to 19.7%~24.3%. Therefore, axle load is the main factor affecting the dynamic response of the tunnel bottom structure.

4.2. Ferroelectric Materials. Ferroelectric materials are widely used in the manufacture of modern electronic devices due to their excellent dielectric properties, piezoelectric properties, and polarization reversibility. The microstructure of ferroelectric materials determines the macroscopic properties of ferroelectric materials to a certain extent, and the simulation of their microstructure is of great significance in material design. At present, the traditional phase field method used to calculate and simulate ferroelectric materials has limitations such as many material parameters, energy potential wells, and unobvious symmetry, which seriously hinder ferroelectric materials, especially the microstructure of new ferroelectric materials.

This paper establishes a theoretical framework for non-traditional phase field simulation of tetragonal and orthogonal ferroelectric phases. Based on the characteristic function of the ferroelectric material variant, use it as the phase field simulation sequence parameter to construct the anisotropic properties of the ferroelectric variant, which presents a multipotential well structure, and use it to replace the traditional phase field method to describe higher-order polynomials in ferroelectric materials. Using the anisotropic properties of ferroelectric variants to replace the polynomial of the internal energy of the traditional phase field method, an unconventional phase field method suitable for tetragonal and orthogonal phase ferroelectric domain structures has been developed. The nontraditional phase field method requires few parameters and can also describe the multipotential well structure of the ferroelectric material variant, and the potential well structure is obvious and the symmetry is obvious.

5. Conclusion

This study found that under different axle loads and surrounding rock conditions, the fatigue damage of the tunnel bottom structure of the single- and double-track heavy-duty railway tunnel is significantly higher than that of the arch wall structure and it is mainly concentrated in the position of the heavy-duty line track and decreases with the increase of depth. The track position of the infill structure began to show damage after 50 years of operation and developed downward; when the operation time exceeds 100 years, the fatigue damage of the inverted structure and the damage of the infill structure are connected. The fatigue damage of the single-track tunnel is always symmetrical, while the

double-track tunnel expands to the bottom of the side trench structure half of the heavy-duty line. Of course, there are some shortcomings in the research of this paper. The data studied in this paper are basically based on simulation results, and no real field investigation has been carried out. In the collected data, the factors that may damage the track in the tunnel are not considered. Completely, the experiments in this article cannot draw very perfect conclusions. This also requires that in today's research, we need to increase the scope of data and conduct real data investigations in order to obtain better research results.

Data Availability

No data were used to support this study.

Conflicts of Interest

There is no potential conflict of interest in this study.

References

- [1] Y. X. Xiao, X. T. Feng, G. L. Feng, H. J. Liu, Q. Jiang, and S. L. Qiu, “Mechanism of evolution of stress-structure controlled collapse of surrounding rock in caverns: a case study from the Baihetan hydropower station in China,” *Tunnelling and Underground Space Technology*, vol. 51, pp. 56–67, 2016.
- [2] M. He, S. Chen, Z. Guo, J. Yang, and Y. B. Gao, “Control of surrounding rock structure for gob-side entry retaining by cutting roof to release pressure and its engineering application,” *Zhongguo Kuangye Daxue Xuebao/Journal of China University of Mining and Technology*, vol. 46, no. 5, pp. 959–969, 2017.
- [3] Q. S. Yan, M. Spiriyagin, Q. Wu, C. Cole, and W. H. Ma, “Feasibility in assessing the dipped rail joint defects through dynamic response of heavy haul locomotive,” *Transportation*, vol. 26, no. 2, pp. 96–106, 2018.
- [4] X. Cai, Y. Zhong, X. Hao, Y. Zhang, and R. Cui, “Dynamic behavior of a polyurethane foam solidified ballasted track in a heavy haul railway tunnel,” *Advances in Structural Engineering*, vol. 22, no. 3, pp. 751–764, 2019.
- [5] Y. Cai, L. Xu, W. Liu, Y. Shang, N. Su, and D. Feng, “Field test study on the dynamic response of the cement-improved expansive soil subgrade of a heavy-haul railway,” *Soil Dynamics and Earthquake Engineering*, vol. 128, p. 105878, 2020.
- [6] P. Liu, K. Wang, and D. Zhang, “Influence of traction and braking operation on wheel-rail dynamic interaction for heavy haul locomotive,” *Zhongguo Tiedao Kexue/China Railway Science*, vol. 38, no. 2, pp. 96–104, 2017.
- [7] D. E. Holder, M. V. Csenge, Y. Qian, M. S. Dersch, J. R. Edwards, and B. J. van Dyk, “Laboratory investigation of the Skf-style fastening system's lateral load performance under heavy freight railroad loads,” *Engineering Structures*, vol. 139, pp. 71–80, 2017.
- [8] Y. Ogawa, B. Hu, C. M. Orofeo et al., “Domain structure and boundary in single-layer graphene grown on Cu(111) and Cu(100) films,” *Journal of Physical Chemistry Letters*, vol. 3, no. 2, pp. 219–226, 2012.
- [9] J. L. Coleman, C. Bolisetti, and A. S. Whittaker, “Time-domain soil-structure interaction analysis of nuclear facilities,” *Nuclear Engineering & Design*, vol. 298, pp. 264–270, 2016.

- [10] X. Xu, M. Fu, Z. Xu, and Z. Chen, "A new lever-type variable friction damper for freight bogies used in heavy haul railway," *Journal of Modern Transportation*, vol. 24, no. 3, pp. 159–165, 2016.
- [11] W. R. Liu, D. Y. Wang, K. Gao, and Z. W. Huang, "Design of distributed cooperative observer for heavy-haul train with unknown displacement," *IET Intelligent Transport Systems*, vol. 11, no. 4, pp. 239–247, 2017.
- [12] Y. Zhang, C. Li, Z. Yu et al., "Comparative test on shape and material of rail used for heavy haul railway of 30 t axle load," *Zhongguo Tiedao Kexue/China Railway Science*, vol. 39, no. 2, pp. 10–17, 2018.
- [13] B. Hu and Z. Luo, "Life-cycle reliability-based assessment of internal stability for mechanically stabilized earth walls in a heavy haul railway," *Computers and Geotechnics*, vol. 101, pp. 141–148, 2018.
- [14] T. Reis, E. D. A. Lima, F. Bertelli, and A. A. dos Santos Junior, "Progression of plastic strain on heavy-haul railway rail under random pure rolling and its influence on crack initiation," *Advances in Engineering Software*, vol. 124, pp. 10–21, 2018.
- [15] J. Dong, Z. H. Wu, X. Li, and H. Y. Chen, "Dynamic response and pile-soil interaction of a heavy-haul railway embankment slope reinforced by micro-piles," *Computers and Geotechnics*, vol. 100, pp. 144–157, 2018.
- [16] G. Duan, L. Chen, Y. Z. Li, and R. He, "Optimisation on empty trains distribution with time window in heavy haul railway," *International Journal of Computing Science and Mathematics*, vol. 9, no. 3, pp. 273–286, 2018.
- [17] K. Smith, "Heavy-haul: navigating the digital railway in Narvik," *International Railway Journal*, vol. 59, no. 7, pp. 4–4, 2019.
- [18] D. Zhang, K. Wang, W. Zhai, and P. Liu, "Effect of unsupported sleepers on the wheel/rail dynamic interaction on heavy-haul railway lines," *Zhendong yu Chongji/Journal of Vibration and Shock*, vol. 36, no. 18, pp. 1–7, 2017.
- [19] L. Zhaohui, M. Yifei, S. Li, and Y. Zhiwu, "Experimental study on fatigue behavior of 8 m low-height reinforced concrete plate-girder of heavy-haul railway," *Journal of Central South University*, vol. 48, no. 9, pp. 2550–2558, 2017.
- [20] D. Wang, J. Zhao, Q. Peng, and X. Wang, "Optimization of train combination schemes at marshalling station in loading end of heavy haul railway," *Tiedao Xuebao/Journal of the China Railway Society*, vol. 39, no. 6, pp. 10–19, 2017.
- [21] H. Wang, T. Fang, Y. U. Xiaoqiang, H. Cao, and J. Guo, "The excavation scheme optimization of beside river interchange ramp unsymmetrical loaded foundation pit," *Journal of Railway Science and Engineering*, vol. 60, no. 2, pp. 64–66, 2016.
- [22] A. Rahmati, L. Faramarzi, and M. Darbor, "Erratum to: squeezing rock conditions at phyllite-slate zone in Golab water conveyance tunnel, Iran: a case study," *Journal of Central South University*, vol. 24, no. 11, pp. 2745–2745, 2017.
- [23] M. T. Semper and R. Bowersox, "Tripping of a hypersonic low-Reynolds-number boundary layer," *AIAA Journal*, vol. 55, no. 3, pp. 1–10, 2017.
- [24] T. Toulkeridis, F. Rodríguez, N. A. Jiménez et al., "Causes and consequences of the sinkhole at El Trébol of Quito, Ecuador – implications for economic damage and risk assessment," *Natural Hazards and Earth System Sciences*, vol. 16, no. 9, pp. 2031–2041, 2016.
- [25] V. D. H. Frank and K. Juchnevic, "The significance of the underground experience: selection of reference design cases from the underground public transport stations and interchanges of the European Union," *Tunnelling and Underground Space Technology incorporating Trenchless Technology Research*, vol. 55, pp. 176–193, 2016.